UC Berkeley
UC Berkeley Previously Published Works

Title

Amorphization in extreme deformation of the CrMnFeCoNi high-entropy alloy.

Permalink

Journal

ISSN

Authors

Zhao, Shiteng
Li, Zezhou
Zhu, Chaoyi
et al.

Publication Date

DOI

Peer reviewed

MATERIALS SCIENCE

Amorphization in extreme deformation of the CrMnFeCoNi high-entropy alloy

Shiteng Zhao[1]*, Zezhou Li[2]*, Chaoyi Zhu[3], Wen Yang[2], Zhouran Zhang[4], David E. J. Armstrong[4], Patrick S. Grant[4], Robert O. Ritchie[1]†, Marc A. Meyers[2]†

Ever-harsher service conditions in the future will call for materials with increasing ability to undergo deformation without sustaining damage while retaining high strength. Prime candidates for these conditions are certain high-entropy alloys (HEAs), which have extraordinary work-hardening ability and toughness. By subjecting the equiatomic CrMnFeCoNi HEA to severe plastic deformation through swaging followed by either quasi-static compression or dynamic deformation in shear, we observe a dense structure comprising stacking faults, twins, transformation from the face-centered cubic to the hexagonal close-packed structure, and, of particular note, amorphization. The coordinated propagation of stacking faults and twins along {111} planes generates high-deformation regions, which can reorganize into hexagonal packets; when the defect density in these regions reaches a critical level, they generate islands of amorphous material. These regions can have outstanding mechanical properties, which provide additional strengthening and/or toughening mechanisms to enhance the capability of these alloys to withstand extreme loading conditions.

INTRODUCTION

Metals have the ability to undergo permanent deformation, a property called ductility, from the Latin ductus or tube. This represents their ability to be shaped into tubes and other complex shapes without fracture. This property has profound consequences in the utilization of metals and their alloys, because they can be formed into many shapes and, during operation, resist the formation and propagation of cracks by plastically deforming their tips, thus blunting them. The mechanisms by which metals exhibit this property have been investigated for 100 years, and a well-developed plasticity theory exists, on the basis of three principal mechanisms: dislocations, twins, and phase transitions. In far rarer occasions, a fourth mechanism can operate, that of the destruction of the crystalline structure by amorphization. We find here the first observation of such deformation by amorphization in an equiatomic high-entropy alloy (HEA).

HEAs were independently developed by Cantor et al. (1) and Yeh et al. (2) in 2004; certain of these alloys, in particular the principally face-centered cubic (fcc) CrCoNi-based HEAs, have been demonstrated to display outstanding strength and ductility, properties that lead to very high fracture toughness (3), i.e., the ability to resist fracture. Thus, many important applications are envisaged for these alloys, with potential revolutionary technological developments (4–6). What is particularly impressive is that this toughness is retained, or even enhanced, at cryogenic temperatures, in contrast to the vast majority of existing metal alloys that display a progressively lower toughness with a decrease in temperature (3, 7). The excellent cryogenic performance of these HEAs indicates that they are potentially more resilient to extreme impact loading, as high strain rates and cryogenic temperatures are usually conjugated in the sense that thermal activation is limited in both scenarios.

CrCoNi-based HEAs exhibit versatile deformation pathways of dislocations-mediated plasticity (8), twinning-induced plasticity (3), and, in specific alloys, transformation-induced plasticity (TRIP) (9). The TRIP effect, which involves an fcc to hexagonal close-packed (hcp) transformation, has already been reported in the three-element CrCoNi alloy (10) and non-equiatomic HEAs (11) because of their markedly lower stacking-fault energies; however, to date, there has been no clear evidence of such a deformation-induced (under ambient pressure) phase change in the classical equiatomic CrMnFeCoNi Cantor HEA. We provide evidence here that under very high strain-rate loading, the TRIP effect can be observed in the Cantor alloy; we show that at high strains and/or elevated strain rates, an additional, yet rarer, deformation mechanism manifests itself, that of solid-state amorphization, which appears to be a characteristic of structural transitions under extreme loading conditions. The authors have noted, while this paper was under review, a very recently published paper on amorphization in a non-equiatomic HEA deformed at cryogenic temperature (12).

RESULTS AND DISCUSSION

We begin with preprocessing our material, the CrMnFeCoNi Cantor alloy, to introduce a high density of dislocations into the annealed grains. An electron backscattered diffraction (EBSD) map in Fig. 1A shows the structure observed after swaging, which subjected the alloy to a nominal strain of 0.8. The deformed grains are clearly visible, as well as banded features within the grains that are indicative of slip bands. Transmission electron microscopy (TEM) (Fig. 1B) confirms that a high density of dislocations was generated. This high level of plastic deformation with its associated high density of defects introduces substantial strengthening in both quasi-static and dynamic conditions.

Figure 1C shows the equivalent stress versus equivalent strain response at a slow strain rate of 10^{-3} s^{-1} and strain rates higher by over several orders of magnitude (1.7×10^3 to 6×10^5 s^{-1}). We have expressed the stresses and strains here as equivalent (Mises) stress and strains to directly compare different deformation regimes by

[1]University of California, Berkeley, Berkeley, CA 94720, USA. [2]University of California, San Diego, La Jolla, CA 92093, USA. [3]Carnegie Mellon University, Pittsburgh, PA 15213, USA. [4]University of Oxford, Oxford OX1 3PH, UK.
*These authors contributed equally to this work.
†Corresponding author. Email: roritchie@lbl.gov (R.O.R.); mameyers@eng.ucsd.edu (M.A.M.)
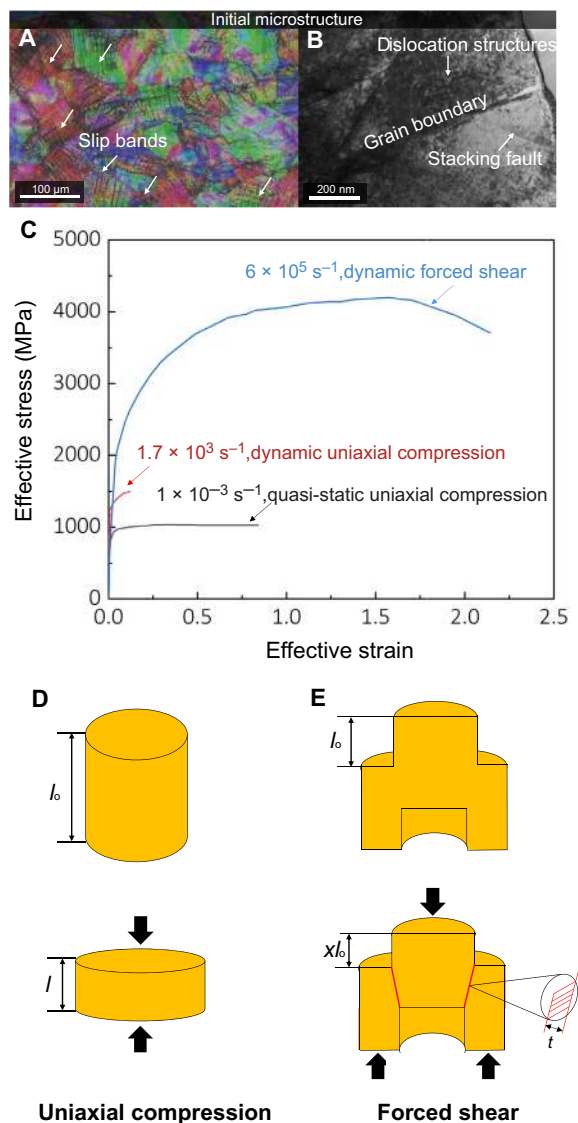
Fig. 1. Initial microstructure, mechanical response, and schematic sample geometry of the as-swaged CrMnFeCoNi HEA. (**A**) EBSD map of the initial microstructure (with inverse pole figure) showing deformed grains with a grain size of ~100 μm. (**B**) TEM micrograph of the as-swaged sample showing a high density of dislocation structures. Note that in both EBSD and TEM characterizations, only very few deformation twins can be observed. This may be attributed to the unique straining pathway of swaging process, which does not favor stress buildup for the activation of twinning. (**C**) Mechanical response, expressed as equivalent stress versus equivalent strain of the as-swaged CrMnFeCoNi HEA subjected to uniaxial quasi-static compression ($\dot{\varepsilon} = 10^{-3}\,s^{-1}$), high strain-rate compression ($\dot{\varepsilon} = 1700\,s^{-1}$), and dynamic shear ($\dot{\gamma} = 6 \times 10^5\,s - 1$). (**D** and **E**) Schematic illustrations of the cylindrical and hat-shaped samples, respectively.

expressing them in terms of the total plastic deformation. For these measurements of the constitutive properties of the alloy, we used uniaxial quasi-static compression (strain rate $\dot{\varepsilon} = 10^{-3}\,s^{-1}$), dynamic uniaxial compression ($\dot{\varepsilon} = 1.7 \times 10^3\,s^{-1}$), and dynamic shear testing (shear strain rate $\dot{\gamma} = 6 \times 10^5\,s^{-1}$). A simple cylindrical geometry (Fig. 1D) was used for the uniaxial compression tests in both quasi-static and dynamic tests, where the strain is uniform throughout the

specimen as the height of the cylinder is reduced by compressive forces. Conversely, to generate the extreme strains at high strain rates, we used an alternative but effective sample geometry, termed the forced hat-shaped geometry, in split Hopkinson pressure bar experiments. This test uses the same externally applied forces but concentrates the deformation into a narrow region (of thickness $t \sim 10\,\mu m$) that serves to create an extreme plastic deformation regime; Fig. 1E shows the cross section of a specimen subjected to such deformation. Details of the test methods and the derivation for equivalent stress and strain in uniaxial compression and simple shear, including the response at 77 K, are provided in Materials and Methods, fig. S1, and additional text in the Supplementary Materials.

As expected, the strength of this alloy increases with strain rate ($10^{-3}\,s^{-1} < 1.7 \times 10^3\,s^{-1} < 6 \times 10^5\,s^{-1}$), as shown earlier for a similar HEA (*13*). The quasi-static and dynamic stress-strain curves both illustrate the high strength of this alloy between 1 and 2 GPa. This, however, does not markedly compromise the ductility as, under quasi-static deformation, the alloy continues to exhibit work hardening up to a strain of 0.8, despite the fact that it had already been predeformed by swaging, to result in a final total strain of 0.95. This dual strength and ductility response serve to ensure a high toughness, even under extreme loading conditions. In the dynamic shear experiment, the equivalent strain is actually much higher, reaching a value of 1.5. Beyond this point, there is a drop of flow stress caused by the local temperature rise due to severe localization, a phenomenon known as adiabatic shear localization, as described in the Supplementary Materials.

TEM revealed complex deformation features in the highly deformed regions after straining at $10^{-3}\,s^{-1}$ (Fig. 2). Under quasi-static loading, a very high density of defects, especially with planar characteristics (Fig. 2A), was observed with high-resolution imaging (Fig. 2B) indicating the cooperation/interaction of multiple mechanisms; deformation twinning and hcp regions can be seen in the fcc microstructure, as respectively shown at higher magnification in Fig. 2 (C and D). A very high density of nanotwins and slip bands can be observed in the low-magnification TEM images, as shown in fig. S2. Of particular importance is the amorphous island seen in Fig. 2B; a high-magnification image in Fig. 2E provides incontrovertible proof of its noncrystalline structure. This amorphous island appears to form at the intersection of hcp and twin packets on intersecting crystallographic planes.

Under dynamic loading, the stress levels are much higher because of strain-rate hardening, and preferred athermal mechanisms, with an even greater preponderance of amorphization, can become active, as illustrated in Fig. 3. The deformed microstructure in the vicinity of a macroscopic shear band generated under dynamic loading provides an ideal location for multiple, well-developed, and amorphous bands (Fig. 3A). The loss of lattice registry can be readily observed, as confirmed by the diffuse scattering nature of the disordered lattice shown by Fourier-transformed diffractograph (Fig. 3C).

At both low and high strain rates, the amorphous regions comprise nanoscale islands, roughly 10 nm in size (Fig. 2E) or bands (Fig. 3, A and C) embedded in regions of concentrated deformation involving dislocations, stacking faults, twins, and hcp phases. These crystalline defects are considered to serve as precursors to the amorphization (*14*). As the deformation temperature is far lower than the melting point of the alloy, the amorphization is clearly a solid-state process. Dynamic experiments were conducted at an initial temperature of 77 K, and the occurrence of amorphization is further
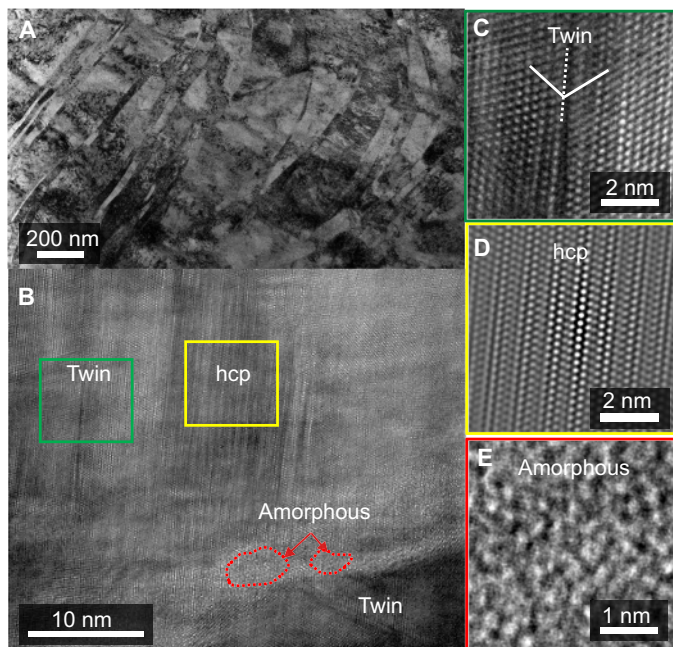
Fig. 2. Deformation microstructure of the swaged CrMnFeCoNi HEA subjected to quasi-static compression. (**A**) TEM bright-field image shows profuse planar deformation features. (**B**) High-resolution TEM micrograph of the heavily deformed area with three distinctive regions of deformation twinning, hcp phase, and an amorphous region. The corresponding lattice images are given in (**C** to **E**), respectively. The hcp region in (D) is Fourier transformation–filtered to maximum the phase contrast, as detailed in the Supplementary Materials. The amorphous island, in (B), is formed at the intersection of hcp and twin bands.

Fig. 3. Deformation microstructure of the CrMnFeCoNi HEA subjected to dynamic compression/shear. (**A**) Bright-field image of the twins, stacking faults, hcp phase, and amorphous bands in the vicinity of the macroscopic adiabatic shear band, as schematically shown in Fig. 1E. (**B**) Selected-area electron diffraction pattern shows the existence of the fcc matrix, twinning spot, and the hcp reflections. (**C**) High-resolution TEM image shows the coexistence of nanoscale twin and the stacking faults (SF). (**D**) Fourier-filtered lattice image of the interface between hcp and fcc phases. (**E**) High-resolution TEM image of the amorphous bands [red square in (A)] and the corresponding fast Fourier–transformed diffractograph.

promoted by this cryogenic deformation (fig. S3), which is attributed to the higher flow stress. We measured the chemical distribution (fig. S4) in the vicinity of the amorphous materials, which shows no apparent chemical segregation, suggesting that the observed amorphization is deformation-induced rather than artifacts induced by sample preparation.

These observations provide irrefutable evidence for amorphization, which, to our knowledge, has never been reported previously in the equiatomic Cantor alloy. The transformation to the hcp phase, ε-martensite, and the amorphous phase can be rationalized in terms of the free energy–based arguments. CrCoNi-based HEAs, such as the current Cantor alloy, are invariably single-phase fcc structures with a low stacking-fault energy, which has been measured to be in the range 20 to 30 mJ m^{-2} (15). To a first approximation, the stacking-fault energy, γ_{sf}, can be estimated as (16)

$$\frac{\gamma_{sf}}{2b} = G_{hcp} - G_{fcc} \tag{1}$$

where G_{hcp} and G_{fcc} are the free energies per unit volume of the hcp and fcc structures, respectively. The stacking-fault energy is expressed per unit area but corresponds to a volume with a constant thickness of ~2b, where b is the Burgers vector. Here, as we are neglecting the contribution of the small magnetism change (ΔG_{mag}) associated with the phase transformation (17), the difference in free energy between the two phases can be directly related to the stacking-fault energy.
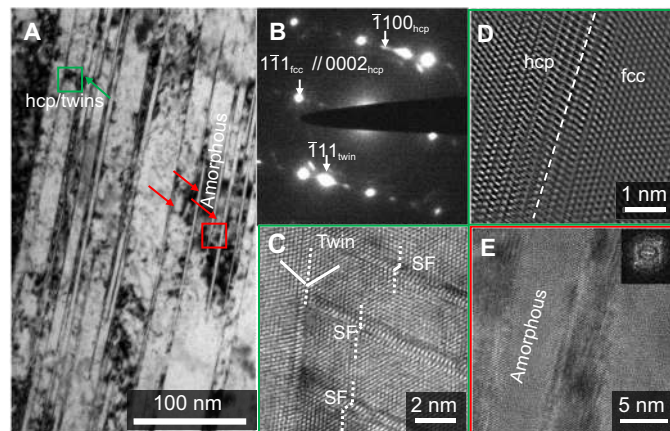
With plastic deformation, the generation of defects such as dislocations and stacking faults increases the energy of the fcc phase. This additional energy due to the defects, G_d, can be expressed as a function of the defect density, ρ, as

$$G_d \sim \frac{\rho \mu b^2}{2} \tag{2}$$

where μ is the shear modulus. When the dislocation density reaches a critical level, the two structures will have the same free energy, creating appropriate conditions for the fcc→hcp transformation

$$G_d + G_{fcc} = G_{hcp} \tag{3}$$

Accordingly, from Eqs. 1, 2, and 3, we can obtain an expression for the critical dislocation density for the transformation in terms of the stacking-fault energy

$$\rho = \gamma_{sf}/(\mu b^3) \tag{4}$$

Using values for the Cantor HEA of b ~ 0.31 nm, μ ~ 80 GPa, γ_{sf} ~ 20 mJ m^{-2}, we predict that the critical dislocation density for the transformation would be ρ ~ 8 × 10^{15} m^{-2}, a value that can be readily achieved through extreme plastic deformation. Thus, we conclude that extreme plastic deformation, achieved by dynamic loading, is sufficient to induce the fcc→hcp transition.

The same energetic argument can be used to explain the amorphization as the amorphous phase is energetically less favorable at ambient conditions. Upon severe plastic deformation, when a higher critical defect concentration is reached, the hcp structure and the heavily deformed fcc matrix can transform, via a solid-state process, to an amorphous phase. We provide details of a mechanism for the evolution of the fraction of amorphous material in the Supplementary Materials. Specifically, the volume fraction of the amorphous

phase depends on the accumulation of stacking faults, twins, and ε-martensite in the deformation bands, whose volume fraction (f_{db}) can be taken to increase with the plastic shear strain (γ) as (*18*)

$$f_{db} = 1 - \exp(-\alpha\gamma) \qquad (5)$$

This expression presumes that the deformation bands are not homogeneously distributed and that the undeformed material is gradually exhausted. Assuming that amorphization occurs at the intersections of the deformation bands, which contain packets of hcp ε-martensite, twins, and stacking faults, the volume fraction of the amorphous material, f_a, should scale with the volume fraction of the intersections of deformation bands, which is related to deformation band fraction to a power of *n*, providing the following relationship

$$f_a = K[1 - \exp(-\alpha\gamma)]^n \qquad (6)$$

The proportionality constant *K*, expressed quantitatively in the Supplementary Materials,, incorporates various material (stacking-fault energy, fraction of ε-martensite in the deformation packets, probability of nucleation of amorphous region at band intersections, thickness of the deformation bands, and others) and external (strain rate and temperature) parameters.

The takeaway from this is that the volume fraction of the amorphous domains should exhibit a sigmoidal relationship with the plastic strain, being almost linear at lower strain and approaching a saturation value (smaller than 1) at a higher strain. However, to determine the parameters for such a relationship requires significant and systematic efforts as displacement-controlled experiments are required, which is nontrivial for dynamic testing.

Nevertheless, one can envisage the broader scenario shown in schematic fashion in Fig. 4. Specifically, as the deformation energy, and accordingly the defect density, is increased, elastic deformation gives way to the generation of dislocations and their motion, then to deformation twinning, then phase transitions until finally in the extreme high strain (and/or high strain rate) regime, where amorphization can occur. The boundary between each mechanism can be loosely delineated by critical defect densities, which shift the free-energy barrier between different phases. The CrMnFeCoNi HEA has a very low stacking-fault energy, which favors defect accumulation during deformation since low stacking-fault energies lead to the dissociation of dislocations with a larger spacing between the partials; this, in turn, acts to severely inhibit the cross-slip of screw dislocations and consequently reduces the probability of dislocation annihilation.

The process of amorphization can release the large deviatoric stresses developed at the intersections of defects (dislocations, stacking faults, and twins) or transformation packets. This release of the deviatoric stresses inhibits the initiation of nano-sized cracks that would otherwise lead to failure. In addition, the amorphous phase should be harder than its crystalline counterpart because dislocations cannot propagate in it. Such are the cases for bulk metallic glasses (*19*) and crystalline/amorphous nanolaminates (*20–22*), which also have extraordinary strength. As a consequence, the absorbed deviatoric strain energy, $W = \int \tau d\gamma$, i.e., the area covered by the shear stress, τ, versus shear strain, γ, curves, of the predeformed materials (~3200 MPa) is approximately twice that of the fully annealed Cantor alloy (~1600 MPa).
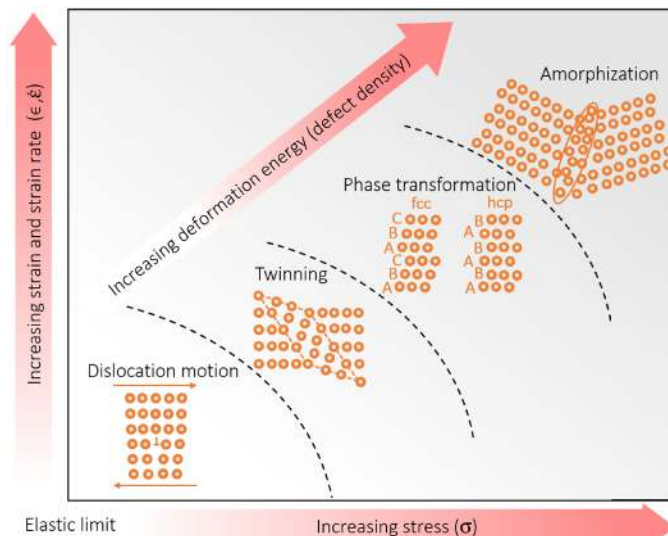

Fig. 4. Proposed hierarchical deformation mechanism paradigm for the equiatomic CrCoNi-based HEAs subjected to increasing degrees of deformation. Elastic deformation, dislocation-mediated plasticity, twinning-induced plasticity, TRIP, and finally solid-state amorphization. Triggering the next mechanism requires the generation of additional defects, i.e., dislocations and/or point defects (vacancies). These multiple mechanisms can interact, leading to a synergy of strengthening processes and a resulting highly complex microstructure.

Thus, we propose that amorphization is actually an additional deformation mechanism manifesting itself in HEAs, which, in addition to dislocation-mediated plasticity, mechanical twinning, and martensitic fcc→hcp phase transitions, provides various pathways for dissipating the imparted strain energy. A proposed microstructural mechanism is shown in fig. S6. Similar phenomenon has been observed in extreme deformation of brittle materials (*23–27*) and takes place during processes such as ball milling (*28*). The versatility and synergy of deformation mechanisms in HEAs render them as viable candidates for extreme load-bearing applications such as in impact penetration, protection, and extreme cryogenic environments. A comparison of the impact resistance of the predeformed HEAs with other structural metals is presented in fig. S5, which clearly shows that the predeformed equiatomic CrMnFeCoNi HEA has a higher absorbed impact strain energy than most commercial structural materials. By tailoring the composition (to further lower the stacking-fault energy) and thermal-mechanical treatment (to introduce higher density of defects), we believe that it will be possible to maximize these beneficial effects to create new and superior metallic alloys designed specifically for extreme loading environments.

MATERIALS AND METHODS
Materials casting, stichometry, and preprocessing
Vacuum induction–melted master ingots of the nominally equiatomic CrMnFeCoNi alloy were supplied by Baosteel, Shanghai, China. The ingots were vacuum induction–melted in an alumina-based crucible at ~1560°C under vacuum (<3×10^{-1} Pa), poured under Ar atmosphere through a 7.2-mm internal-diameter ZrO_2 nozzle into a two-stage commercial purity N_2 atomizer, and spray-formed at a melt flow rate of ~0.55 kg s^{-1} into cylindrical billets at a spray distance of 600 mm at Oxford University. The starting and

as-sprayed alloy compositions were measured by AMG Superalloys (UK) using induction-coupled plasma optical emission spectroscopy, as shown in table S1. Spray forming led to a slight reduction in Mn concentration by preferential evaporation during vacuum-induction melting and a typical increase in N_2 concentration. The as-sprayed billet was sectioned using high-pressure water jet cutting and then machined into 9-mm-diameter and 150-mm-length rods that were swaged to 5-mm diameter in four progressive stages of reduction, giving a cold work strain of ~80%.

Quasi-static and dynamic mechanical testing

Compression and shear specimens were extracted from the as-swaged HEA rods and subjected to quasi-static uniaxial compression (10^{-3} s^{-1}), dynamic uniaxial compression (1.7×10^3 s^{-1}), and dynamic shear experiments (local strain rate of 6×10^5 s^{-1}) through standard procedures. Specifically, an Instron universal testing machine was used for quasi-static compression (up to a strain of 0.8), and a split Hopkinson pressure bar with the hat-shaped specimens was used for generating a shear strain up to 1.5.

For the cylindrical sample shown in Fig. 1D, if compression reduces the overall length from l_o to xl_o, the normal nominal strain is simply calculated by the expression $(l_o - xl_o)/l_o$.

For the hat-shaped specimen shown in Fig. 1E, when it is subjected to compression, the top of the "hat" is pushed down by the force in such a manner that the length is reduced from l_o to xl_o, in a similar manner to the cylindrical specimen. However, the strain is now localized in a narrow region with width t with the shear strain calculated as $(l_o - xl_o)/t$. Since $t \sim 10$ μm, which is much less than $l_o \sim 5$ mm, the strain is much higher than the one in in the simple cylindrical geometry; it reaches a value above 1.5.

Transmission electron microscopy

Conventional TEM was conducted using a JEOL-2800 microscope operated at 200 kV. High-resolution atomic imaging was performed on a Titan 80-300 microscope with a monochromator and operated at an accelerating voltage of 300 kV. Site-specific TEM samples were site-specifically lifted out from the region of interest on the bulk materials using a Thermo Fisher Scientific HELIOS focused ion beam (FIB) machine. Thinning of the sample was conducted using a focused Gallium beam sequence at sequential accelerating voltages of 30, 16, 8, and 5 kV, until the foil was electron transparent. The sample was then final polished by low-voltage (700 V) argon ion milling on a Fischione 1040 NanoMill to get rid of the undesirable FIB damage. Energy-dispersive x-ray spectroscopy (EDX) was conducted using a Thermo Fisher Scientific Titan 80-300 microscope equipped with SuperEDX detectors. Image processing was conducted using Gatan's Digital Micrograph software. In some cases (Figs. 2D and 3, D and E), a fast Fourier transformation of the high-resolution TEM images was performed to obtain diffraction information of the region. In Figs. 2D and 3D, the Fourier-filtered images, which illuminate the diffused scattering, are presented to better display the phase contrast of the sample.

SUPPLEMENTARY MATERIALS

Supplementary material for this article is available at http://advances.sciencemag.org/cgi/content/full/7/5/eabb3108/DC1

REFERENCES AND NOTES

1. B. Cantor, I. T. H. Chang, P. Knight, A. J. B. Vincent, Microstructural development in equiatomic multicomponent alloys. *Mater. Sci. Eng. A* **375–377**, 213–218 (2004).

2. J.-W. Yeh, S.-K. Chen, S.-J. Lin, J.-Y. Gan, T.-S. Chin, T.-T. Shun, C.-H. Tsau, S.-Y. Chang, Nanostructured high-entropy alloys with multiple principal elements: Novel alloy design concepts and outcomes. *Adv. Eng. Mater.* **6**, 299–303 (2004).

3. B. Gludovatz, A. Hohenwarter, D. Catoor, E. H. Chang, E. P. George, R. O. Ritchie, A fracture-resistant high-entropy alloy for cryogenic applications. *Science* **345**, 1153–1158 (2014).

4. D. B. Miracle, J. D. Miller, O. N. Senkov, C. Woodward, M. D. Uchic, J. Tiley, Exploration and development of high entropy alloys for structural applications. *Entropy* **16**, 494–525 (2014).

5. Y. Zhang, T. T. Zuo, Z. Tang, M. C. Gao, K. A. Dahmen, P. K. Liaw, Z. P. Lu, Microstructures and properties of high-entropy alloys. *Prog. Mater. Sci.* **61**, 1–93 (2014).

6. Z. Li, S. Zhao, R. O. Ritchie, M. A. Meyers, Mechanical properties of high-entropy alloys with emphasis on face-centered cubic alloys. *Prog. Mater. Sci.* **102**, 296–345 (2019).

7. B. Gludovatz, A. Hohenwarter, K. V. S. Thurston, H. Bei, Z. Wu, E. P. George, R. O. Ritchie, Exceptional damage-tolerance of a medium-entropy alloy CrCoNi at cryogenic temperatures. *Nat. Commun.* **7**, 10602 (2016).

8. Z. Zhang, H. Sheng, Z. Wang, B. Gludovatz, Z. Zhang, E. P. George, Q. Yu, S. X. Mao, R. O. Ritchie, Dislocation mechanisms and 3D twin architectures generate exceptional strength-ductility-toughness combination in CrCoNi medium-entropy alloy. *Nat. Commun.* **8**, 14390 (2017).

9. Z. Li, K. Gokuldoss Pradeep, Y. Deng, D. Raabe, C. Cem Tasan, Metastable high-entropy dual-phase alloys overcome the strength-ductility trade-off. *Nature* **534**, 227–230 (2016).

10. C. Niu, C. R. LaRosa, J. Miao, M. J. Mills, M. Ghazisaeidi, Magnetically-driven phase transformation strengthening in high entropy alloys. *Nat. Commun.* **9**, 1363 (2018).

11. E. P. George, W. A. Curtin, C. C. Tasan, High entropy alloys: A focused review of mechanical properties and deformation mechanisms. *Acta Mater.* **188**, 435–474 (2020).

12. K. Ming, W. Lu, Z. Li, X. Bi, J. Wang, Amorphous bands induced by low temperature tension in a non-equiatomic CrMnFeCoNi alloy. *Acta Mater.* **188**, 354–365 (2020).

13. Z. Li, S. Zhao, S. M. Alotaibi, Y. Liu, B. Wang, M. A. Meyers, Adiabatic shear localization in the CrMnFeCoNi high-entropy alloy. *Acta Mater.* **151**, 424–431 (2018).

14. S. Zhao, E. N. Hahn, B. Kad, B. A. Remington, C. E. Wehrenberg, E. M. Bringa, M. A. Meyers, Amorphization and nanocrystallization of silicon under shock compression. *Acta Mater.* **103**, 519–533 (2016).

15. T. M. Smith, M. S. Hooshmand, B. D. Esser, F. Otto, D. W. McComb, E. P. George, M. Ghazisaeidi, M. J. Mills, Atomic-scale characterization and modeling of 60° dislocations in a high-entropy alloy. *Acta Mater.* **110**, 352–363 (2016).

16. S. Zhao, G. M. Stocks, Y. Zhang, Stacking fault energies of face-centered cubic concentrated solid solution alloys. *Acta Mater.* **134**, 334–345 (2017).

17. L. Vitos, P. A. Korzhavyi, J. O. Nilsson, B. Johansson, Stacking fault energy and magnetism in austenitic stainless steels. *Phys. Scr.* **77**, 065703 (2008).

18. G. B. Olson, M. Cohen, Kinetics of strain-induced martensitic nucleation. *Metall. Trans. A.* **6**, 791–795 (1975).

19. T. C. Pekin, J. Ding, C. Gammer, B. Ozdol, C. Ophus, M. Asta, R. O. Ritchie, A. M. Minor, Direct measurement of nanostructural change during in situ deformation of a bulk metallic glass. *Nat. Commun.* **10**, 2445 (2019).

20. Y. Wang, J. Li, A. V. Hamza, T. W. Barbee Jr., Ductile crystalline–amorphous nanolaminates. *Proc. Natl. Acad. Sci. U.S.A.* **104**, 11155–11160 (2007).

21. W. Guo, E. A. Jägle, P.-P. Choi, J. Yao, A. Kostka, J. M. Schneider, D. Raabe, Shear-induced mixing governs code formation of crystalline-amorphous nanolaminates. *Phys. Rev. Lett.* **113**, 035501 (2014).

22. J. Wang, Q. Zhou, S. Shao, A. Misra, Strength and plasticity of nanolaminated materials. *Mater. Res. Lett.* **5**, 1–19 (2017).

23. R. Jeanloz, T. J. Ahrens, J. S. Lally, G. L. Nord Jr., J. M. Christie, A. H. Heuer, Shock-produced olivine glass: First observation. *Science* **197**, 457–459 (1977).

24. M. Chen, J. W. McCauley, K. J. Hemker, Shock-induced localized amorphization in boron carbide. *Science* **299**, 1563–1566 (2003).

25. B. Grocholski, S. Speziale, R. Jeanloz, Equation of state, phase stability, and amorphization of SnI$_4$ at high pressure and temperature. *Phys. Rev. B.* **81**, 094101 (2010).

26. S. K. Deb, M. Wilding, M. Somayazulu, P. F. McMillan, Pressure-induced amorphization and an amorphous–amorphous transition in densified porous silicon. *Nature* **414**, 528–530 (2001).

27. D. Machon, F. Meersman, M. C. Wilding, M. Wilson, P. F. McMillan, Pressure-induced amorphization and polyamorphism: Inorganic and biochemical systems. *Prog. Mater. Sci.* **61**, 216–282 (2014).

28. C. C. Koch, Amorphization of single composition powders by mechanical milling. *Scr. Mater.* **34**, 21–27 (1996).

29. U. Andrade, M. A. Meyers, K. S. Vecchio, A. H. Chokshi, Dynamic recrystallization in high-strain, high-strain-rate plastic deformation of copper. *Acta Metall.* **42**, 3183–3195 (1994).

30. Z. Li, S. Zhao, B. Wang, S. Cui, R. Chen, R. Z. Valiev, M. A. Meyers, The effects of ultra-fine-grained structure and cryogenic temperature on adiabatic shear localization in titanium. *Acta Mater.* **181**, 408–422 (2019).

31. A. K. Zurek, The study of adiabatic shear band instability in a pearlitic 4340 steel using a dynamic punch test. *Metall. Mater. Trans. A* **25**, 2483–2489 (1994).

32. L. Anand, W. A. Spitzig, Initiation of localized shear bands in plane strain. *J. Mech. Phys. Sol.* **28**, 113–128 (1980).

33. K. Eswar Prasad, B. Li, N. Dixit, M. Shaffer, S. N. Mathaudhu, K. T. Ramesh, The dynamic flow and failure behavior of magnesium and magnesium alloys. *JOM* **66**, 291–304 (2014).

Amorphization in extreme deformation of the CrMnFeCoNi high-entropy alloy

Shiteng Zhao, Zezhou Li, Chaoyi Zhu, Wen Yang, Zhouran Zhang, David E. J. Armstrong, Patrick S. Grant, Robert O. Ritchie and Marc A. Meyers